

POLARIMETRIC WAVELET FRACTAL REMOTE SENSING PRINCIPLES FOR SPACE MATERIALS (PREPRINT)

George C. Giakos, et al.

**University of Akron
Research Services and Sponsored Programs
302 Buchtel Common
Akron, OH 44325-0002**

4 June 2012

Journal Article

APPROVED FOR PUBLIC RELEASE; DISTRIBUTION IS UNLIMITED.



**AIR FORCE RESEARCH LABORATORY
Space Vehicles Directorate
3550 Aberdeen Ave SE
AIR FORCE MATERIEL COMMAND
KIRTLAND AIR FORCE BASE, NM 87117-5776**

REPORT DOCUMENTATION PAGE			<i>Form Approved</i> OMB No. 0704-0188	
Public reporting burden for this collection of information is estimated to average 1 hour per response, including the time for reviewing instructions, searching existing data sources, gathering and maintaining the data needed, and completing and reviewing this collection of information. Send comments regarding this burden estimate or any other aspect of this collection of information, including suggestions for reducing this burden to Department of Defense, Washington Headquarters Services, Directorate for Information Operations and Reports (0704-0188), 1215 Jefferson Davis Highway, Suite 1204, Arlington, VA 22202-4302. Respondents should be aware that notwithstanding any other provision of law, no person shall be subject to any penalty for failing to comply with a collection of information if it does not display a currently valid OMB control number. PLEASE DO NOT RETURN YOUR FORM TO THE ABOVE ADDRESS.				
1. REPORT DATE (DD-MM-YYYY) 04-06-2012		2. REPORT TYPE Journal Article		3. DATES COVERED (From - To) 14 Aug 2009 – 4 Jun 2012
4. TITLE AND SUBTITLE Polarimetric Wavelet Fractal Remote Sensing Principles for Space Materials (Preprint)			5a. CONTRACT NUMBER FA8718-09-C-0040	
			5b. GRANT NUMBER	
			5c. PROGRAM ELEMENT NUMBER 62601F	
6. AUTHOR(S) George C. Giakos, Richard H. Picard, Phan D. Dao, Peter N. Crabtree, Patrick J. McNicholl, Jeff Petermann, Suman Shrestha, Chaya Narayan, and Stefanie Marotta			5d. PROJECT NUMBER 1010	
			5e. TASK NUMBER PPM00005963	
			5f. WORK UNIT NUMBER EF004457	
7. PERFORMING ORGANIZATION NAME(S) AND ADDRESS(ES) The University of Akron Research Services and Sponsored Programs 302 Buchtel Common Akron, OH 44325-0002			8. PERFORMING ORGANIZATION REPORT NUMBER	
9. SPONSORING / MONITORING AGENCY NAME(S) AND ADDRESS(ES) Air Force Research Laboratory Space Vehicles Directorate 3550 Aberdeen Ave SE Kirtland AFB, NM 87117-5776			10. SPONSOR/MONITOR'S ACRONYM(S) AFRL/RVBYC	
			11. SPONSOR/MONITOR'S REPORT NUMBER(S) AFRL-RV-PS-TP-2012-0056	
12. DISTRIBUTION / AVAILABILITY STATEMENT Approved for public release; distribution is unlimited. (377ABW-2012-0338 dtd 20 March 2012)				
13. SUPPLEMENTARY NOTES Submitted for publication by SPIE Defense, Security, and Sensing, Baltimore, Maryland, 23-27 April 2012. Government Purpose Rights.				
14. ABSTRACT A new remote sensing approach based on polarimetric wavelet fractal detection principles is introduced and the Mueller matrix formalism is defined, aimed at enhancing the detection, identification, characterization, and discrimination of unresolved space objects at different aspect angles. The design principles of a multifunctional liquid crystal monostatic polarimetric ladar are introduced and related to operating conditions and system performance metrics. Backscattered polarimetric signal contributions from different space materials were detected using a laboratory ladar testbed, and then analyzed using techniques based on wavelets and fractals. The depolarization, diattenuation, and retardance of the materials were estimated using Mueller matrix decomposition for different aspect angles. The outcome of this study indicates that polarimetric fractal wavelet principles may enhance the capabilities of the ladar to provide characterization and discrimination of unresolved space objects.				
15. SUBJECT TERMS Space Surveillance, Ladar Remote Sensing, Physical Algorithm, Space Materials Characterization, Mueller Matrix Decomposition, Polarimetric Wavelet Fractal Analysis				
16. SECURITY CLASSIFICATION OF:			17. LIMITATION OF ABSTRACT Unlimited	18. NUMBER OF PAGES 16
a. REPORT Unclassified	b. ABSTRACT Unclassified	c. THIS PAGE Unclassified		
				19b. TELEPHONE NUMBER (include area code)

Polarimetric Wavelet Fractal Remote Sensing Principles for Space Materials

*George C. Giakos,***Richard. H. Picard, ****Phan D. Dao, ****Peter N. Crabtree, ****Patrick J. McNicholl, *Jeff Petermann, *Suman Shrestha, *Chaya Narayan, and **Stefanie Marotta

*Dept. of Electrical and Computer Engineering,

**Dept. of Biomedical Engineering

The University of Akron, Akron, OH 44325-3904, USA

***ARCON Corporation, Waltham, MA 02451

****Air Force Research Laboratory, Space Vehicles Directorate
Kirtland AFB, NM 87111, USA

ABSTRACT

A new remote sensing approach based on polarimetric wavelet fractal detection principles is introduced and the Mueller matrix formalism is defined, aimed at enhancing the detection, identification, characterization, and discrimination of unresolved space objects at different aspect angles. The design principles of a multifunctional liquid crystal monostatic polarimetric lidar are introduced and related to operating conditions and system performance metrics. Backscattered polarimetric signal contributions from different space materials were detected using a laboratory lidar testbed, and then analyzed using techniques based on wavelets and fractals. The depolarization, diattenuation, and retardance of the materials were estimated using Mueller matrix decomposition for different aspect angles. The outcome of this study indicates that polarimetric fractal wavelet principles may enhance the capabilities of the lidar to provide characterization and discrimination of unresolved space objects.

Keywords: Space Surveillance, Lidar Remote Sensing, Physical Algorithm, Space Materials Characterization, Mueller Matrix Decomposition, Polarimetric Wavelet Fractal Analysis,

1. INTRODUCTION

Polarimetric sensing and imaging offer unique advantages for a wide range of detection and classification problems due to the intrinsic potential for high contrast in different polarization components of the backscattered light. Indeed, polarized imaging can yield high-specificity images under high-dynamic range and extreme condition scenarios, in scattering media, or cluttered environments, offering at the same instance information related to the object material composition and its surface characteristics^{1-11,18-30}. Active polarimetric sensors using laser sources offer predictable illumination levels, polarimetric filtering to minimize specular reflections, and the ability to operate independent of sunlight illumination and temperature. In addition, an active illumination source is aligned with the detector, allowing more direct light to reach the objects, which in turn reduces shadows and increases visibility, reducing at the same time the false-alarm rate. Although active sensors offer superior signal-to-noise ratio (SNR) and convenience of use, they are larger, more costly and complex to build, and consume more power. While there exist a number of effective space surveillance detection and imaging spectral-polarimetric technologies and methodologies, further progress is both necessary and possible toward more efficient and reliable detection, identification, characterization, and discrimination of small, low-contrast, unresolved space objects. Accurate sensing of small and distant satellites as well as the discrimination of these satellites from natural near-earth objects and man-made debris is still a challenging and important space remote-sensing task, along with the prediction of interactions between and threats to these space objects. New remote sensing detection principles based on polarimetric wavelet fractal detection principles aimed at enhancing the detection, identification, characterization, and discrimination of unresolved space objects at different aspect angles were previously introduced^{9-10, 28}. The combination of polarimetry and wavelet-fractal analysis yields enhanced knowledge of the spatial-temporal-frequency characteristics of backscattered lidar signals from space objects²⁸.

Wavelets are a family of transforms whose basis functions are of short duration and finite energy¹⁰. There is a large variety of wavelet functions available. Various wavelet families exhibit different degree of spatial compactness and smoothness. In contrast to the Fourier transform, which effectively assumes that the signal is stationary at time scales of

interest, the wavelet transform determines a signal's frequency content as a function of time. The result is a trade-off between localization in the time and frequency domains. In fact, the time and frequency domain analysis provided by the wavelet transform provides the opportunity to explore the nature of transient signals by representing the time varying spectral response through time-frequency maps, as well as to analyze signals for conditions where responses change significantly in amplitude during experiments. Wavelets have found applications in situations that require analysis over very short time durations or where information is localized, and have been combined with polarimetry for characterization of biological samples under transmissive geometry. Similarly, fractal analysis is based on the original fractal framework introduced by Mandelbrot¹⁵. Fractal geometry is the geometry of self-similarity in which an object appears to look similar at different scales. The key concept of fractal analysis relies on the fact that a fractal dimension can be considered as a quantitative measure of object surface heterogeneity because of its inherent self-similarity features. The fractal dimension can be interpreted as measure of heterogeneity of a set of points on a plane, or in space, for instance, a measure of surface roughness. The signals obtained in this study are 1-D polarimetric signals and hence a fractal dimension applicable to 1-D signals must be applied. There are several methods for computation of fractal dimension¹⁷, such as the "Box Counting Method," the "Multiresolution Box-counting Method," the "Katz Method," the "Sevcik Method," the "Higuhi Method," the "Regularization Method," the "Maximum Entropy Method," and others. Typically, the box counting method is based on the method of covering the part, whose fractal dimension is to be calculated, with a number of square boxes and hence the number of boxes $N(r)$ of size r is calculated which is required to cover the part. As the size of the square r (side of a square) approaches zero, the area covered by the square boxes will converge to a measure of the curve which can be expressed mathematically as

$$D_B = \lim_{r \rightarrow 0} \left(\log(N(r)) / \log(1/r) \right) \quad (1)$$

In Practice, the fractal dimension is calculated by fitting the log-log plot of $\log(N(r))$ versus $\log(1/r)$ (least squares method) and then calculating the slope of the plot. The slope of the plot gives the fractal dimension of the signal, which gives

$$\log(N(r)) = D_B \log(1/r) + C \quad (2)$$

Here, D_B is the fractal dimension or box counting fractal dimension of the signal. The method requires 2-D processing of the curve at various grid sizes, which increases the computational time. In this study we used an improved version of the box dimension method, namely the "Multiresolution Box-counting Method."¹⁷ The applied technique estimates the fractal dimension with less computational time and is insensitive to wave amplitude, therefore providing enhanced robustness for real-time applications. The physical algorithm and applied metrics of this study on the material characterization of space materials is shown in Fig. 1, with reference to polysilicon, a material found to exhibit higher diffused scattering characteristics, depolarization, and fractal dimension, with respect to amorphous silicon.

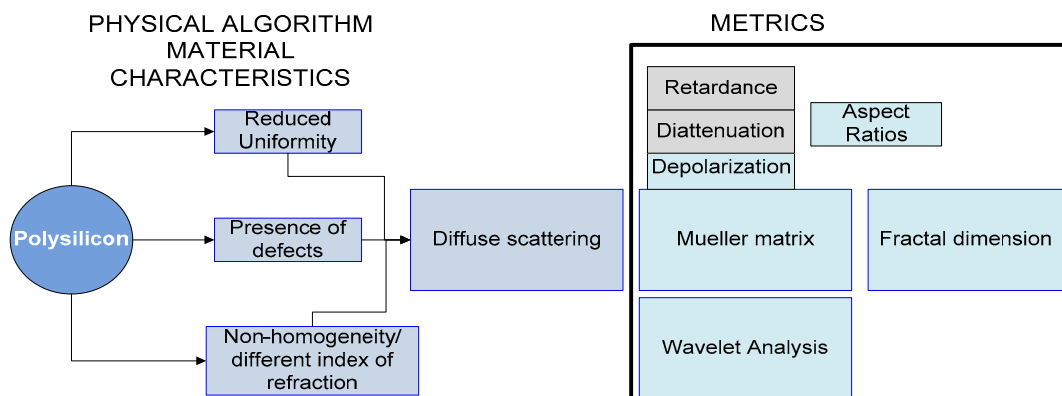


Figure 1. Physical algorithm and applied metrics

2. SPACE MATERIALS

In this study, two space materials used in solar panel structures are examined, namely, amorphous silicon and polycrystalline silicon (polysilicon). Amorphous silicon is an entirely non-crystalline form of silicon that can be thought of as grains the size of individual atoms. On the other hand, standard polysilicon consists of 0.5 to 1 micrometer discrete grains, or crystals, of mono-crystalline silicon that generate regions of highly uniform crystal structures, therefore, of different refractive indices, separated by grain boundaries. Both amorphous silicon and polysilicon solar cell samples were analyzed using confocal microscopy. Example images of these samples are shown in Figures 2 and 3, respectively. The amorphous silicon solar sample has a characteristic size of approximately 2 mm, while the polysilicon solar cell sample has grain sizes in the micrometer range. This explains the enhanced specular characteristics associated with amorphous silicon rather with polysilicon, which instead exhibits pronounced diffuse scattering.

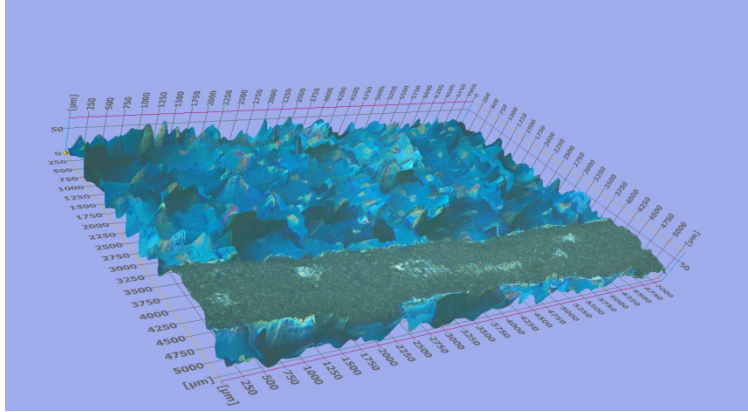


Figure 2. Confocal microscopy image of an amorphous silicon solar cell sample

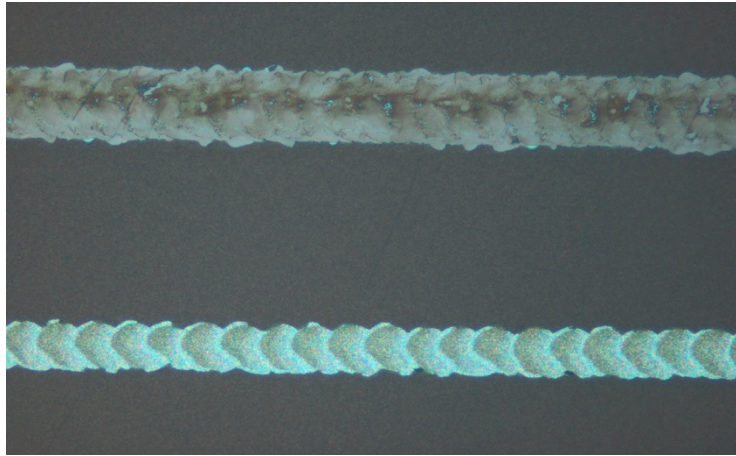


Figure 3. Confocal microscopy image of a polysilicon solar cell sample

3. MUELLER MATRIX DECOMPOSITION AS FUNCTION OF THE ASPECT ANGLE

Mueller matrix decomposition into a sequence of three matrix factors, namely, depolarization, retardance, and diattenuation, was originally proposed by Shih-Yau Lu, et al.³². This concept can be expanded for Bidirectional Reflectance Distribution Function (BRDF) applications by expressing them in terms of the aspect angle of an object, θ , so that

$$M(\theta) = M_{\text{depol}}(\theta) M_{\text{ret}}(\theta) M_{\text{diat}}(\theta) \quad (3)$$

$M_{\text{depol}}(\theta)$ accounts for the depolarizing effects of the medium, $M_{\text{ret}}(\theta)$ accounts for the retardance effects of linear birefringence and optical activity, and $M_{\text{diat}}(\theta)$ describes the effects of linear and circular dichroism. From these matrices the diattenuation, retardance, and depolarization characteristics of the medium are readily determined.

The depolarization is quantified in terms of the depolarization index, P_D , according to

$$P_D(\theta) = \text{Dep}(M(\theta)) = 1 - \frac{\sqrt{\left(\sum_{i,j} m_{ij}^2(\theta)\right) - m_{00}^2(\theta)}}{\sqrt{3}m_{00}(\theta)} \quad (4)$$

where $m_{ij}(\theta)$ are the MM elements as a function of the aspect angle. From the decomposed retardance matrix, $M_{\text{ret}}(\theta)$, the total retardance, R , which includes the effects of both linear and circular birefringence, can be expressed as

$$R(\theta) = \cos^{-1} \left(\frac{\text{tr}(M_{\text{ret}}(\theta))}{2} - 1 \right) \quad (5)$$

where $\text{tr}(M_{\text{ret}}(\theta))$ is the trace of the retardance matrix. The diattenuation, d , is dependent on the first row vector of the MM. This vector describes differential attenuation for both linear and circular polarization states and the diattenuation can be expressed in terms of it as

$$d(\theta) = \frac{1}{m_{00}(\theta)} \times \sqrt{m_{01}^2(\theta) + m_{02}^2(\theta) + m_{03}^2(\theta)} \quad (6)$$

4. WAVELET ANALYSIS OF THE POLARIZATION STATES

The 16 polarimetric states for amorphous silicon, polysilicon, Mylar, and Kapton were analyzed using continuous wavelet transforms (CWTs) and their respective scalograms were plotted. In this study, the particular wavelet was chosen from the Daubechies family, namely, the ‘db4’ wavelet. In order to understand the frequency and time resolution of the analysis better, we pick a line of coefficients for particular scale values from low and high scale regions respectively. The scale values themselves were picked based on the scalograms of the polarization states. High frequencies were observed predominantly about a scale value of 150 while low frequencies were observed about a scale value of 450 on a range of 512 scales. In order to average noise and to get a better picture of the signal variation with the scale value chosen, we choose a range of scale values about the chosen scale line of interest and average the scale line coefficients in this range. For this study, we choose a range of 5 lines about the scale value of interest. The lowest frequency was calculated as follows:

- Each signal has 2500 sample points corresponding to 5 cycles
- Each cycle of signal therefore has 500 points
- Each signal was captured at a rate of 10^5 samples/second
- Signal frequency (signal rate/number of samples per cycle) = $(10^5/500) = 200$ Hz, which is also the modulation frequency of the laser.

5. FRACTAL DIMENSION OF SPACE MATERIALS USING MULTIREOLUTION BOX COUNTING METHOD

Let us consider a continuous time signal. The signal needs to be sampled at a sampling rate of $1/f_s$ at least twice the Nyquist rate to discretize the signal. Let $s = \{s(1), s(2), \dots, s(N)\}$ be the discrete time signal sampled at a sampling

frequency of f_s and having N samples. Each sample points can be represented by $(x(i), y(i))$, where $i = 1$ to N . The abscissa($x(i)$) and the ordinate($y(i)$) values of the samples are now known. The applied algorithm consists of the following steps:

Step 1: Consider two discrete samples of the signal $s(i)$ and $s(i+1)$. The time difference between the two samples is given by $dt = x(i+1) - x(i)$, and the height difference between the two samples is $h = y(i+1) - y(i)$. The width of the rectangle box required to cover the two points is $r = dt$ and the number of square boxes of size r required to cover the two points is $b = |h|/r$. The same procedure is repeated for all other points of the signal with the value of h changing and r being the same. Then the number of boxes of size r required to cover all the samples in the signal is given by $b(i) = |h(i)|/r$. The total number of boxes required to cover the curve at the resolution r is $B(r) = \sum(b(i))$, where $i = 1$ to $N-1$. This is shown in Figure 3(a).

Step 2: Now the time resolution is increased to $r = dt = x(i+2) - x(i)$, i.e., the size of the box is increased. The same procedure is repeated and the number of boxes of size r required to cover all the samples is calculated.

Step 3: The same procedure is now repeated for different time resolutions and the number of boxes required to cover the sample points with the respective box size is calculated. A log-log plot of $B(r)$ with $1/r$ is plotted. The plot is linear fitted using least square method and the slope of the linear fit denotes the fractal dimension of the 1-D signal. The algorithm is depicted graphically in Fig. 4(a) and 4(b).

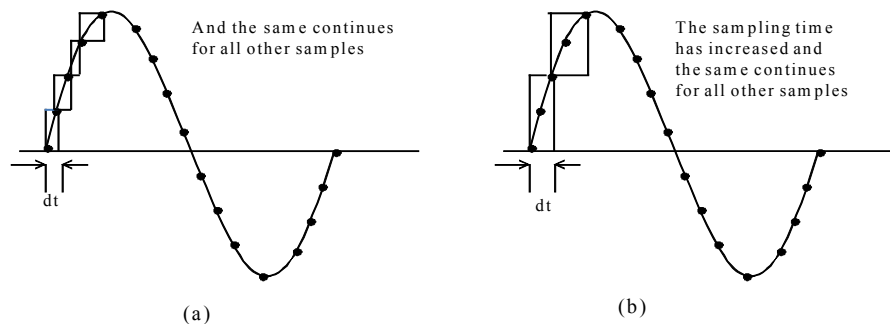


Figure 4. Explanation of multiresolution technique for 1-D signals for two cases: (a) multiresolution technique at the finest resolution, and (b) multiresolution technique with the resolution increased.

To implement the multiresolution box counting algorithm for 1-D signals from space materials, the discrete samples of the signals are known sampled at $t = 10^{-6}$ sec with $N = 2500$. Since the signal is sampled at very small time durations, the sampling time is increased to $T = 10t$ and thus gives $N = 250$ samples to process. The similar algorithm is applied for 10 grid sizes for all the materials (to be consistent) and the corresponding fractal dimensions of the signals are calculated.

6. EXPERIMENTAL ARRANGEMENT AND PROCEDURES

The goal of this study was to characterize remotely several types of space materials based on the detection of distinct backscattered signatures, by interrogating the objects with different polarization states so as to obtain complete characterization of the MM of the objects in terms of depolarization, diattenuation, and retardance. The following space materials were studied: a) amorphous silicon (a-silicon)-based solar panel, and b) polycrystalline silicon (polysilicon) solar panel.

The experimental arrangement used in this study is described by Figure 5.

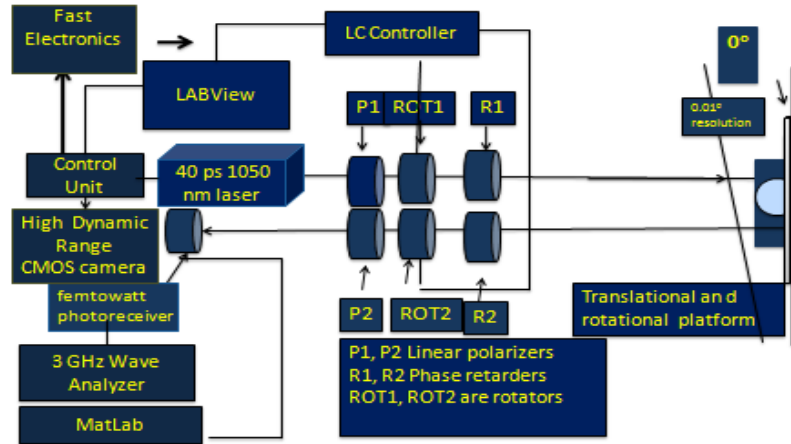


Figure 5. The U.S. Air Force Research Laboratory (AFRL) multifunctional imaging platform

The U.S. Air Force Research Laboratory (AFRL) liquid crystal (LC) polarimetric multifunctional imaging platform comprises a complete polarimeter capable of deriving the full 16 element Mueller Matrix (MM) of an object using LC devices. The system is highly automated by utilizing NI Labview software to control the devices and measurement states, and perform a detailed calibration of the optical system. It is fully reconfigurable and scalable providing enhanced multifunctional surveillance capabilities through dedicated spatial, timing and spectral modules, supported by advanced calibration and image pre-processing and post-processing techniques developed in-house. The LC polarimeter consists of the following components:

1. **Generator arm:** The incident laser light is initially linearly polarized by a **fixed polarizer** at $+45^\circ$.
2. The light then passes through a **compensated variable retarder** (polarization **rotator**) that is capable of producing all linear polarization states, including but not limited to horizontal, vertical, and $\pm 45^\circ$.
3. The light then passes through a **variable retarder**, which is capable of producing right and left circularly polarized light.
4. The light then impinges on the target, and the diffusely reflected light is collected by the analyzer arm.
5. **Analyzer arm:** The analyzer arm consists of the same components as the input arm except in reverse order and with the fixed polarizer set at -45° . The experimental arrangement of the generator-analyzer arms is shown in Figure 6.

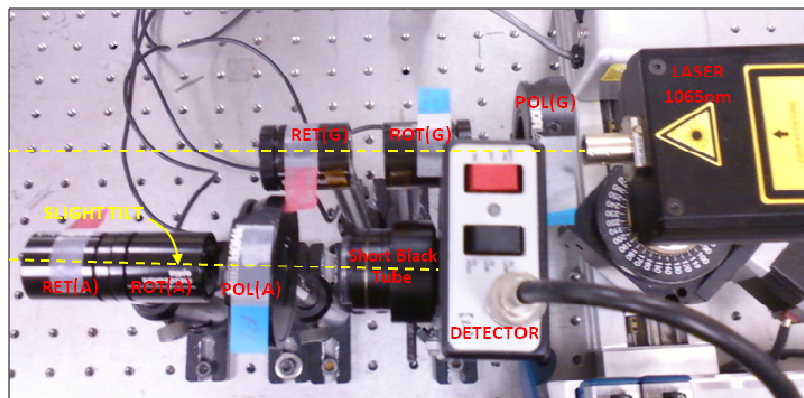


Figure 6. Experimental geometry of the backscattering polarimetric system

In these sets of experiments, 1065 nm laser pulses with a PRR of 200 Hz were transmitted through the generator system illuminating the space object material. The light was then backscattered in the direction of the analyzer arm and detected by a New Focus 2151 femtowatt photodetector. The waveforms were acquired through a NI Labview data acquisition system (DAS), and then processed using Excel and Matlab subroutines. Amorphous silicon and polysilicon solar panels were mounted on a rotating stage. As shown in Figure 6, the receiver was placed off-axis with respect to the normal incidence of laser beam on the solar panel at a fixed scattering angle of 2.46° . Rotation was achieved by way of a stepper motor with a resolution of 0.01° .

6.1 Calibration Procedure

A technique called the Method of Swings [35] was used in conjunction with the Null Intensity Method [19]. This involves setting Polarizer(Analyzer) at some angle $\pm \theta$ about the suspected null. When the intensities are identical the true location of the Null is known. The full calibration procedure applied to this study is the following:

- 1) Use Null Intensity Method to determine the LC voltage which corresponds to the desired rotation or retardation to within $1/10^{\text{th}}$ of a volt.
- 2) Use the “Method of Swings” to further adjust the LC voltage for maximum precision.
- 3) Verify the proper calibration of the state by varying the θ of Polarizer(A) according to the method described in [19].

A comparison of the experimentally estimated 16 polarization states with reported accuracy (for the calculation of MM of Air, Linear Horizontal Polarizer (LHP) and Linear Vertical Polarizer (LVP) with ideal and measured values) is shown in Table I.

Table I. Calibration and System Accuracy

Element	Ideal Mueller Matrix			Measured Mueller Matrix			Element Variances		
	Air	LVP	LHP	Air	LVP	LHP	Air	LVP	LHP
m11	1	1	1	1.000	1.000	1.000	0.0	0.0	0.0
m12	0	-1	1	0.001	-0.969	0.974	1.3E-6	985.4E-6	666.7E-6
m13	0	0	0	-0.043	0.057	-0.029	1.8E-3	3.3E-3	838.7E-6
m14	0	0	0	-0.012	-0.001	-0.011	141.3E-6	760.3E-9	110.8E-6
m21	0	-1	1	0.001	-0.968	0.971	1.1E-6	1.0E-3	813.5E-6
m22	1	1	1	0.992	0.960	0.971	60.0E-6	1.6E-3	827.2E-6
m23	0	0	0	0.002	-0.058	-0.028	2.8E-6	3.3E-3	771.1E-6
m24	0	0	0	0.045	0.001	-0.010	2.0E-3	258.7E-9	93.2E-6
m31	0	0	0	0.070	-0.096	0.011	4.9E-3	9.2E-3	115.9E-6
m32	0	0	0	-0.016	0.094	0.011	269.8E-6	8.8E-3	117.6E-6
m33	1	0	0	0.991	0.019	0.005	86.4E-6	343.3E-6	24.7E-6
m34	0	0	0	-0.053	0.015	-0.001	2.8E-3	239.5E-6	1.2E-6
m41	0	0	0	0.039	0.001	-0.009	1.5E-3	1.0E-6	82.8E-6
m42	0	0	0	0.009	-0.002	-0.009	82.5E-6	6.1E-6	81.3E-6
m43	0	0	0	-0.022	0.023	-0.002	500.2E-6	533.9E-6	4.8E-6
m44	1	0	0	0.989	0.023	0.003	123.5E-6	527.2E-6	10.4E-6
STANDARD DEVIATION:							29.9E-3	43.2E-3	16.9E-3

7. EXPERIMENTAL RESULTS AND DISCUSSION

Experiments were performed under quasi-monostatic backscattered polarimetric geometry using amorphous silicon and polysilicon material samples. Backscattered polarimetric intensities as a function of the aspect angles of the solar panel samples were recorded and the Mueller matrices of the samples were estimated. By applying the MM decomposition technique (Eq. 3), the depolarization, diattenuation, and retardance, matrices for a-silicon and polysilicon were estimated and plotted as function of the aspect angle, as shown in Figures 7(a) and 7(b), respectively. The experimental results of Fig. 7 indicate that polysilicon exhibits higher depolarization than amorphous silicon. This is attributed to its pronounced diffuse scattering characteristics because of its microcrystalline structure, presence of defects and none uniformity. On the other hand, the retardance exhibits a Lambertian pattern in both samples. The diattenuation of the amorphous silicon

and polysilicon increases initially with increasing the aspect angle of the object, while polysilicon exhibits a distinct pattern which was confirmed through repetitive measurements; the symmetric decrease of the diattenuation at larger aspect angle of the polysilicon may be attributed to the drop of the signal-to-noise ratio because of polysilicon's intrinsic pronounced scattering characteristics.

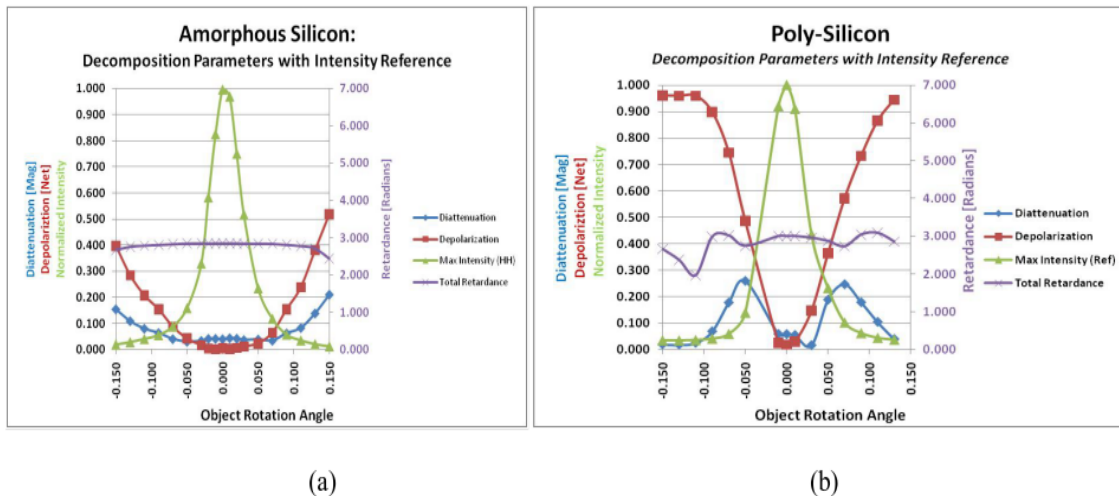


Figure 7. Decomposition matrices of two types of space materials: (a) amorphous silicon, and (b) polysilicon

Analysis of the experimentally determined polarization states of the space materials was performed using wavelet transforms according to [12]. Scalograms were calculated for an aspect angle ranging between -0.07 to $+0.07$ degrees, with scales from 2 to 512, in step size of 2; representative examples for selected cases are shown in Figure 8.

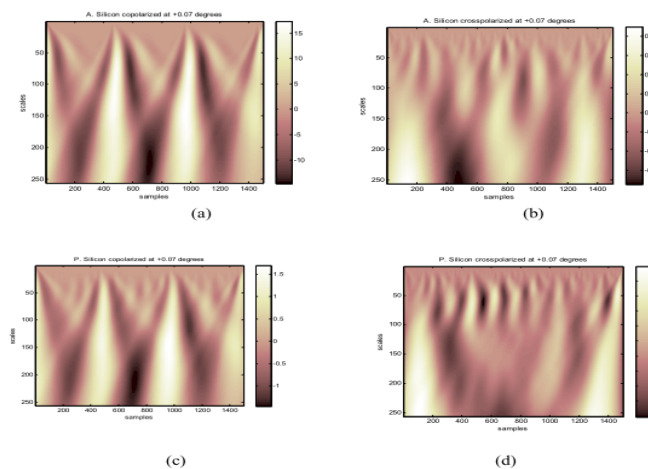


Figure 8. Scalograms corresponding to amorphous silicon and polysilicon at an aspect angle of -0.07 degrees. Amorphous silicon: (a) copolarized geometry and (b) crosspolarized geometry. Polysilicon: (c) copolarized geometry and (d) crosspolarized geometry

Distinct signatures are observed reflecting mainly the specular nature of amorphous silicon and the diffuse scattering characteristics of polysilicon; diffuse scattering contributes to blur or “ghost” patterns, at the low and high frequencies. It has been observed that blur or “ghost patterns increases with increasing the aspect angle of the object, as diffuse reflectance becomes dominant; again, polysilicon exhibits these effects to a greater degree due to its higher

depolarization and scattering yield. In search of distinct signatures from these two space panel materials, a line of coefficients for particular scale values from low-scale (high-frequency) and high-scale (low-frequency) regions, respectively, was selected and plotted. The scale values themselves were picked based on the scalograms of the polarization states. High frequencies were observed predominantly about a scale value of 150 while low frequencies were observed about a scale value of 450 on a range of 512 scales. In order to average noise and obtain a better representation of the signal variation with the scale value chosen, a range of scale values about the chosen scale line of interest (148 to 152) or (448 to 452) was selected; specifically, a range of 5 lines about the scale value of interest was chosen. An average of high-scale (low-frequency) line coefficients for amorphous silicon and polysilicon, both for selected polarization stated, is shown in Figure 9.

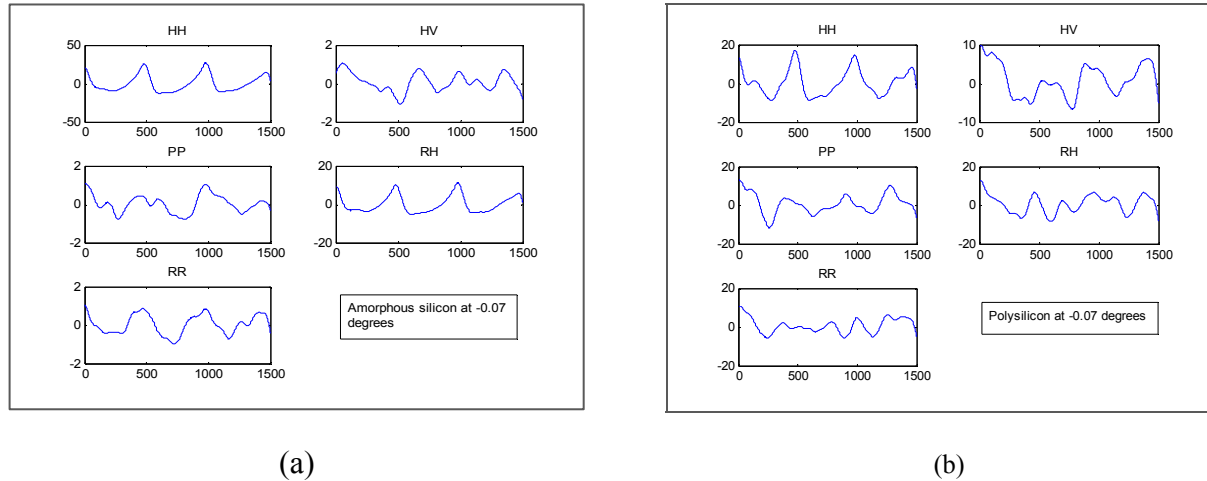


Figure 9. Average of high-scale (low-frequency) line coefficients for amorphous silicon and polysilicon: (a) amorphous silicon; HH, HV, PP, RH, RR states, and (b) polysilicon: HH, HV, PP, RH, RR states

Signal similarity has been quantified in terms of the correlation coefficients of different polarimetric scalograms each one representing one of the 16 polarization states of a space material sample at a fixed aspect angle. A pictorial representation of the autocorrelation between polarization for amorphous silicon and polysilicon-based solar panel samples, at two different aspect angles, -0.07 and 0 degrees are shown in Fig. 10.

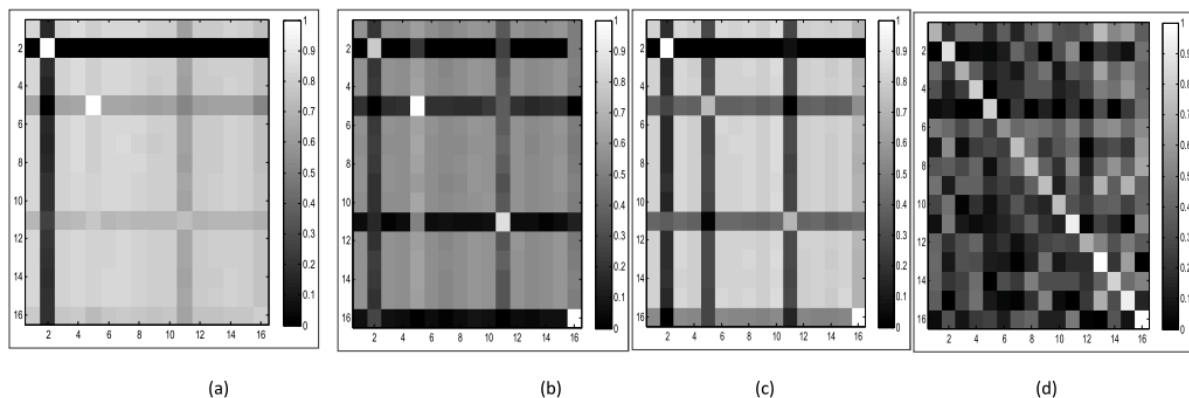
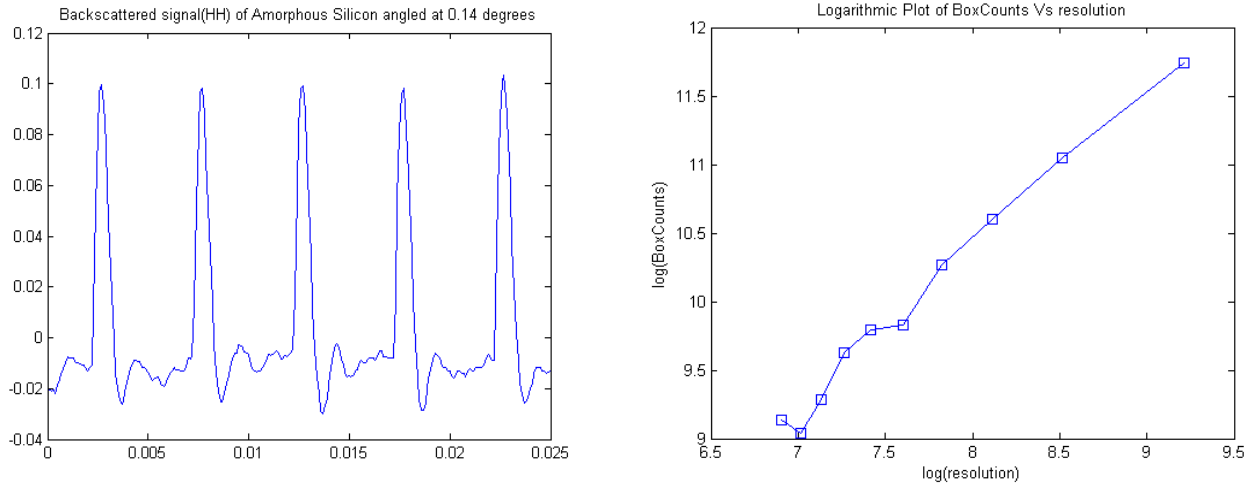


Figure 10. Autocorrelations among signals representing the 16 states for amorphous silicon and polysilicon at two different aspect angles: (a) amorphous silicon at 0 degrees, (b) polysilicon at 0 degrees, (c) amorphous silicon at -0.07 degrees, and (d) Polysilicon at -0.07 degrees

The x and y axes represent the 16 polarization states linearly and uniformly distributed. The white color represents a value of 1 indicating a 100% likeness, while progressively darker shades indicate a proportionally reduced degree of likeness. In other words, the whiter regions represent high correlations. Each pixel value represents the correlation coefficient between polarization states at fixed material, and fixed angle. By observing Figure 9, it is seen that amorphous silicon and polysilicon exhibit more signal similarity (whiter regions) at 0 degrees than at -0.07, within certain regions of interest (ROI). This would be explained based on diffused scattering characteristics of polysilicon which becomes pronounced with increasing aspect angles. The fractal dimension is calculated by fitting (best linear fit) the log-log plot of $\log(N(r))$ and $\log(1/r)$ (least squares method) and then calculating the slope of the plot. The slope of the plot gives the fractal dimension of the signal, according to Eq. 2. The logarithmic plots of box counts ($N(r)$) versus resolution $1/r$ for amorphous silicon and polysilicon, are shown in Figure 11.

(a). Amorphous Silicon at 0.14 degrees: Backscattered signal and Box counts vs. resolution



(b) Polysilicon at 0.14 degrees: Backscattered signal and Box counts vs. resolution

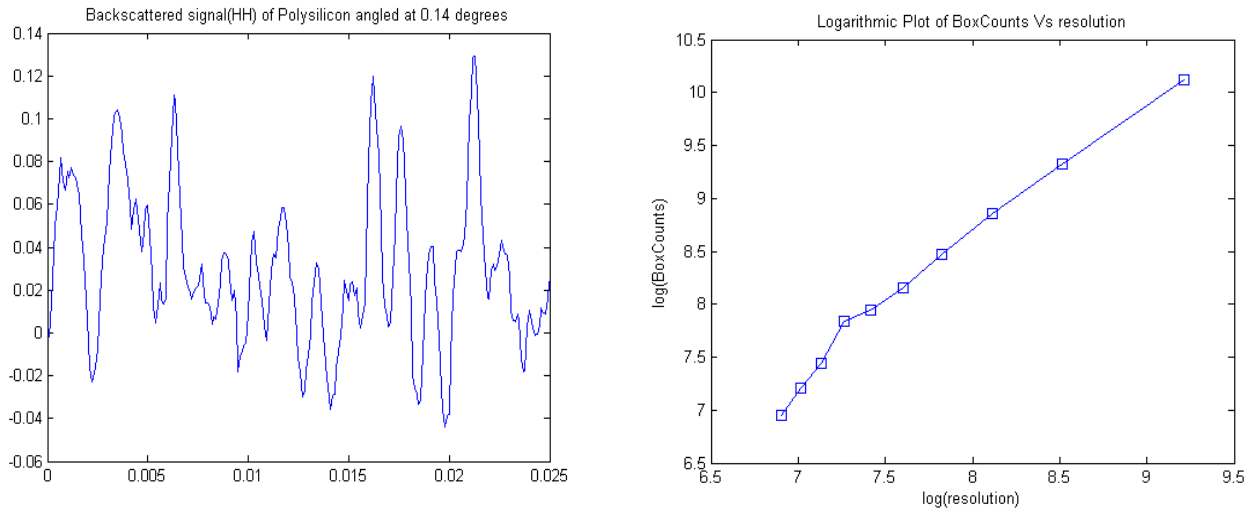


Figure 11. (a) Backscattered contributions and logarithmic plots of box counts ($N(r)$) versus resolution $1/r$ at an aspect angle of 0.14° for amorphous silicon under collinearly polarized geometry; (b) backscattered contributions and logarithmic plots of box counts ($N(r)$) versus resolution $1/r$ at an aspect angle of 0.14° for polysilicon under collinearly polarized geometry

A comparison of fractal dimensions among different space material for selected polarization states and aspect angles is shown in Table II:

TableII Comparison of fractal dimensions among different space materials

Materials/Angles	0 degrees		0.14 degrees (predominantly diffused reflectance)	
	HH	HV	HH	HV
Amorphous Silicon	1.189644534	1.435106471	1.289284645	1.427184698
Mylar	1.203158205	1.222856222	1.197328496	1.269531896
Kapton	1.224981172	1.355107509	1.290935866	1.389688974
Polysilicon	1.148899471	1.453745597	1.335139104	1.512163558

The fractal dimensions of the amorphous silicon, polysilicon, Kapton, and Mylar, are plotted for distinct polarization states in Figure 12, at two different aspect angles.

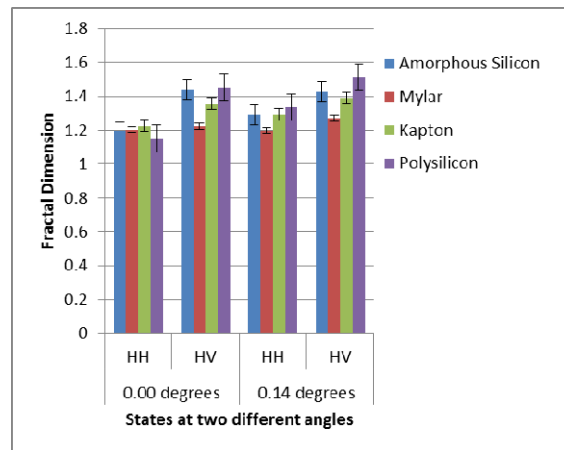


Figure 12. Plot of fractal dimension of space materials at two different polarimetric states and two different aspect angles

8. CONCLUSION

The experimental results of this study indicate that media with highly diffuse scattering characteristics, such as polysilicon, exhibit higher depolarization, and fractal dimension, with respect to amorphous silicon which exhibit rather pronounced specular characteristics. The outcome of this experimental study indicates that polarimetric wavelet fractal principles applied to ladar return signals may provide an enhanced capability to characterize and discriminate unresolved space objects.

ACKNOWLEDGEMENTS

G. C. Giakos and R. H. Picard gratefully acknowledge that this study was performed under contract with the U.S. Air Force Research Laboratory (AFRL). The authors acknowledge the valuable contributions of Professor A. Karim, and Dr. J. Marszalek, Polymer Engineering, The University of Akron, for providing confocal microscopy images of the space material samples.

References

- [1] C. Pohl and J. L. van Genderen, "Multisensor image fusion in remote sensing: concepts, methods and applications", *I Remote Sensing*, 19:5, pp. 823-854, 1998.
- [2] Jed Khoury, Charles L. Woods, Joseph Lorenzo, John Kierstead, Dana Pyburn, and Sandip K. Sengupta, "Resolution limits in imaging lidar systems", *Applied Optics*, Vol. 45, No. 4, 1 February 2006.
- [3] MIT Lincoln Laboratory, "Geiger-Mode Avalanche Photodiodes for 1.5- μ m Sensitive Focal Planes", August 2005.
- [4] Neelam Gupta: Fused Spectropolarimetric Visible Near-IR Imaging, pp. 21-26, 2003.
- [5] P.M. Alsing, D.A. Cardimona, D.H. Huang, T. Apostolova, W.R. Glass, C.D. Castillo, "Advanced space-based detector research at the Air Force Research Laboratory", *Infrared Physics & Technology* 50, 89–94, 2007.
- [6] Jonathan W. Cambell, "Laser Orbital Debris Removal and Asteroid Deflection", Occasional Paper No. 20, Air University, Maxwell Air Force Base, December 2000.
- [7] D.H. Goldstein, and D.B. Chenault, "Near Infrared Imaging Polarimetry", *Proc. SPIE* 4481, pp. 30-31, 2001.
- [8] A.B. Mahler, P. Smith, R. Chipman, G. Smith, N. Raouf, A. Davis, B. Hancock, G. Gutt, and D. J. Diner, "High-accuracy Spectropolarimetric Imaging using Photoelastic Modulator-based, Cameras with Low-Polarization Coatings", NASA Technology Conference 2007.
- [9] G.C. Giakos, Quarterly Report #4, AFRL, 2010.
- [10] George C. Giakos, Richard. H. Picard, Phan D. Dao, Peter N. Crabtree, Patrick J. McNicholl, "Polarimetric Wavelet Phenomenology of Space Materials", *IEEE International Conference on Imaging Systems and Techniques*, Batu Ferringhi, Malaysia, IEEEExplore, pp.1-6, 17-18 May 2011.
- [11] G. Giakos, R. Picard, P. Dao, and P. Crabtree, "Object detection and characterization by monostatic lidar Bidirectional Reflectance Distribution Function (BRDF) using polarimetric discriminants," *SPIE*, vol. 7482, 748208-748208-10, 2009.
- [12] J.B. Buckheit and D.L. Donoho, "Wavelab and Reproducible Research," Dept. Statist., Stanford Univ., Stanford, CA, 1995. Available at: <http://wwwstat.stanford.edu/wavelab>.
- [13] I. Daubechies, "Orthogonal bases for compactly supported wavelets," *Commun. Pure Appl. Math*, vol. 41, pp. 909-996, 1992.
- [14] Y. Katznelson, *An Introduction to Harmonic Analysis*, New-York, Dover, 1976.
- [15] B.B. Mandelbrot, *The Fractal Geometry of Nature*, W.H. Freeman and Co., New York, 1977.
- [16] I.M. Johnstone and B.W. Silverman, "Wavelet threshold estimators for data with correlated noise," *J. Roy. Statist. Soc.*, vol. 59, pp. 319-351, 1997.
- [17] B.S Raghavendra, and D.Narayana Dutt, Computing Fractal Dimension of Signals using Multiresolution Box-counting Method, *International Journal of Information and Mathematical Sciences*, 6 (1). pp. 50-65, 2011.
- [18] E. Collett, *Polarized Light*, Marcel Dekker, 1993.
- [19] Goldstein and Collett, *Polarized Light*, CRC Press, 2003.
- [20] G.C. Giakos, Quarterly Report #3, AFRL, 2010.
- [21] D.B. Chenault, and J.L. Pezzaniti, "Polarization Imaging through Scattering Media," vol. 4133, *SPIE* 2000.
- [22] R.A. Chipman, "Polarimetry," Ch 22 of *Handbook of Optics*, 2nd ed., vol. 2, New York, McGraw Hill, 2001.
- [23] G.C. Giakos, Quarterly Report #4, AFRL, 2010.
- [24] J.R. Shell II, S.D. Brown, M.G. Gartley, and J.R. Schott, *Fundamentals of Polarimetric Remote Sensing*, SPIE Press, 30 March 2009.
- [25] D.B. Chenault, and J.L. Pezzaniti, "Polarization Imaging through Scattering Media", vol. 4133, *SPIE* 2000
- [26] G. Giakos, R. Picard, and P. Dao, "Superresolution multispectral imaging polarimetric space surveillance LADAR sensor design architectures", *SPIE* vol. 207, pp. 71070B-71070B-12, 2008.
- [27] G. C. Giakos, "Advanced Detection, Surveillance, and Reconnaissance Principles", *Proc. IEEE International Workshop on Measurement Systems for Homeland Security*, pp. 6 – 10, Orlando, FL, 2005.
- [28] M.B.K. Reddy, *Advanced Object Characterization and Monitoring Techniques Using Polarimetric Imaging*, MS Thesis, The University of Akron, 2009.
- [29] G.C. Giakos, US Airforce Research Laboratory AFRL) Contract, "Detection of LADAR Targets using MultiDomain Mueller Matrix Polarimetric Bidirectional Reflectance Distribution Function (BRDF) and Fractals for Space Surveillance", 2009.
- [30] Azzam, R. M. A., "Photopolarimetric Measurement of the Mueller Matrix by Fourier Analysis of a Single Detected Signal," *Optical Letters*, Vol. 2, pp.148-150, 1978.

DISTRIBUTION LIST

DTIC/OCP

8725 John J. Kingman Rd, Suite 0944

Ft Belvoir, VA 22060-6218

1 cy

AFRL/RVIL

Kirtland AFB, NM 87117-5776

2 cys

Official Record Copy

AFRL/RVBYC/Willa Inbody

1 cy

This page intentionally left blank.